

Real-Time Debonding Monitoring of Composite Repaired Materials via Electrical, Acoustic, and Thermographic Methods

S.A. Grammatikos, E.Z. Kordatos, T.E. Matikas, and A.S. Paipetis

(Submitted March 8, 2013; in revised form July 18, 2013; published online August 27, 2013)

The electrical properties of composite materials have been thoroughly investigated recently for the detection and monitoring of damage in carbon fiber-reinforced polymers (CFRPs) under mechanical loading. Carbon nanotubes are incorporated in the polymer matrix of CFRPs for the enhancement of their electrical properties. The electrical properties have shown to be sensitive to the damage state of the material and hence their monitoring provides the profile of their structural deterioration. The aim of the paper is the cross-validation and benchmarking of an electrical potential change monitoring (EPCM) technique against acoustic emission (AE) and lock-in thermography (LT). All techniques successfully identified damage and its propagation. Thermography was more efficient in quantifying damage and describing dynamically the debond topology, as it provided full 2D imaging of the debond in real time. EPCM was successful in providing quantitative information on debond propagation and its directionality. AE provided consistent information on damage propagation. All techniques identified three stages in the fatigue life of the inter-rogated coupons. The representation of the fatigue behavior as a function of life fraction, the correlation of AE data with EPCM and LT data, and most importantly the consistent behavior of all tested coupons allowed for both the direct and indirect cross-correlation of all employed methodologies, which consistently identified all aforementioned fatigue life stages.

Keywords aerospace composites, non-destructive evaluation, repair

1. Introduction

Carbon fiber-reinforced polymers (CFRPs) have been very popular as structural materials in aerostructures due to their high specific mechanical properties (Ref 1, 2). Their increased use in commercial aircrafts such as the Airbus A350, A380, and the recent Boeing 787 (Dreamliner) accentuates the need for efficient repair technologies. Aircraft structures undergo complex loading during operation which leads to gradual structural degradation. The repair of a deteriorated structural component is often considered as the optimum option as compared to replacement. In an early work by Baker (Ref 3), the possibility of bonded repair was investigated. Bonded repair comprised an adhesively bonded composite patch on a cracked surface (Ref 4). Adhesive bonding of the patch is superior to mechanical fastening as undesirable stress concentrations which inevitably occur at the fastening positions are not present (Ref 3, 5). However, there is a dire need to enhance the reliability of bonded repair in order for it to qualify as a repair practice for structural components. In-service monitoring of the

“structural health” of a repaired component is the safest route toward (i) assessing its structural integrity, (ii) enhancing the confidence of the aircraft industry toward bonding technologies, and ultimately (iii) reducing overall operational costs for safe airborne structures (Ref 6).

The electrical properties of CFRPs have been examined as a means of assessing the structural integrity of composite structures in order to identify their possible structural degradation. The electrical continuity of the conductive reinforcement has been shown to be highly sensitive to changes in the structure in the presence of external mechanical load (Ref 7). Every disruption of the electrical paths formed by the conductive reinforcement in the bulk CFRP is directly reflected as a change in the electrical resistivity of the material (Ref 8-13). This effect may be enhanced via the dispersion of a conductive phase of a scale lower than that of the primary reinforcement. Carbon nanotubes (CNTs) (Ref 14-16) and polyaniline (Ref 17, 18) render typical epoxy matrices antistatic or even conductive. Consequently, the bulk CFRP becomes more electrically isotropic as it acquires conduction in other directions than those provided by the carbon reinforcement. The modified-matrix composites retain their electrical anisotropy, but electrical properties are significantly enhanced, e.g., in the through thickness direction after the inclusion of the secondary conductive phase (Ref 7, 10, 14, 16, 19). This nanoincorporation is reported to positively affect the electrical sensitivity of the CFRP materials to strain or damage (Ref 7).

Thus, electrical resistance change monitoring (ERCM) or electrical potential change monitoring (EPCM) methodologies have been extensively investigated in the recent years with the aim of providing a measure of damage accumulation under mechanical load (Ref 7, 10, 19-22). The major advantage of

S.A. Grammatikos, E.Z. Kordatos, T.E. Matikas, and A.S. Paipetis, Department of Materials Engineering, University of Ioannina, 45110 Ioannina, Greece. Contact e-mail: paipetis@cc.uoi.gr.

these techniques is that no external sensing elements are needed as the variation of the resistivity is an inherent material property and consecutively the principle structure is not aggravated (Ref 23-25). However, various parameters, e.g., contact resistance, local resistivity variation, and/or geometrical parameters, increase the uncertainty of electrical property-based techniques. As a result, efficient benchmarking technologies have to be employed to verify the ERCM or EPCM results.

Within the aim of this work, the potential of EPCM is investigated for the monitoring of initiation and propagation of damage in composite repaired materials. CFRP panels with an artificially induced circular notch were repaired using an adhesively bonded composite patch. The bonding repair efficiency was assessed in real time using EPCM, lock-in thermography (LT), and acoustic emission (AE) under tension-tension cyclic loading. AE and LT were utilized in order to benchmark the results provided by EPCM. AE is employed for the localization of critical and subcritical damage or the damage between the repair and the parent material as well as the damage observed from the presence of an artificially induced circular notch. LT is employed as a full-field method to visualize and quantify debonding and stress concentrations around the artificially induced notch. Post-mortem optical stereoscopic examination of the failed coupons was employed to verify the results provided by the aforementioned methods.

2. Overview of Benchmarking Techniques

Infrared thermography (IrT) has been shown to be capable of identifying and monitoring service-induced damage in composite materials (Ref 26, 27). In the case of load-bearing structures, IrT can be employed to monitor damage initiation and propagation due to mechanical loading (Ref 28, 29). On one hand, stresses induced during mechanical loading lead to temperature variations due to the thermoelastic effect. On the other hand, irreversible processes such as defect nucleation and growth result in heat release which may be manifested locally as a hot spot. Moreover, these defects which accumulate and/or grow during loading act as heat traps which delay locally the cooling down process. Due to the above, the thermal gradients on the material surface can be recorded in order to assess the stress and the damage state of the material (Ref 30, 31). LT is based on the detection with an IR camera of thermal waves generated onto the surface of a material subjected to periodical (usually sinusoidal) thermal excitation. The principle of LT lies in the synchronization of the thermal camera with the source of heating (Ref 32-37). The resultant thermal transient of the generated thermal waves which is recorded in real time is analyzed via fast Fourier transform to provide phase and amplitude images. The phase image is time dependent, while the amplitude relates more to the thermal diffusivity of the thermal waves (Ref 32). In the case of cyclic mechanical loading, the thermal waves which are generated are a result of the thermomechanical coupling through the thermoelastic effect. The thermoelastic effect for a thermally isotropic solid is well described by the following equation (Eq 1):

$$\Delta T = (-\alpha/\rho C_p)T\Delta\sigma = K_m T\Delta\sigma \quad (\text{Eq 1})$$

where ρ is the mass density, C_p the specific heat and constant pressure, α the coefficient of thermal expansion (CTE), T the absolute temperature, ΔT the change in temperature in Kelvin

degrees, K_m the thermoelastic coefficient, and $\Delta\sigma$ the change in the sum of principal stresses. For a typical CFRP plate, CTE varies or even changes sign for the longitudinal and transverse direction (Ref 38), and as a result, the thermoelastic effect is different in the two principle directions (Ref 39, 40). For the plane stress and an orthotropic solid, it is more accurate to refer to express the temperature change as

$$\Delta T = -(T/\rho C_p)(\alpha_L\Delta\sigma_L + \alpha_T\Delta\sigma_T) = K_{mL}T\Delta\sigma + K_{mT}T\Delta\sigma, \quad (\text{Eq 2})$$

where the subscripts L and T denote the longitudinal and transverse directions, respectively. What is typically shown by Eq 2 is that the thermoelastic response of a loaded material is the sum of the thermoelastic response of the stresses in the two principal directions, which cannot be distinguished. Hence, depending on the sum of the parameters in Eq 2, the temperature of a thermally anisotropic material either increases or decreases during tension and vice versa during compression (Ref 41, 42)

Along with IrT, AE is a well-established technique which is capable of providing information on the structural deterioration of a material during mechanical loading. Local irreversible energy release due to damage such as crack initiation and propagation is manifested as transient acoustic waves. These may be recorded by sensors, acoustically coupled on the material under study. AE activity is directly affected by the characteristics of the induced stress field and, as a result, parameters such as duration and energy may be employed to provide a real-time structural degradation spectrum (Ref 43, 44). More analytically, acoustic signals emitted during mechanical loading of materials are attributed to damage due to mechanical deformation. Piezoelectric transducers placed on the surface of the material capture the elastic waves released during crack propagation incidents (Ref 45). Information about the location and the structural severity is available through acoustic signal tracking (Ref 46). Different forms of damage in composite materials under mechanical loading have been identified by many researchers (Ref 47, 48).

3. Experimental

3.1 Material Preparation

The CFRP coupons used for this study consisted of composite plates (substrate) with a circular notch drilled in the middle to simulate service-induced damage. The area of the notch was subsequently repaired using a tapered patch which was hand laid-up on the notched plate and subsequently cured in place. The circular notch was chosen as representative of damage in real conditions, as it is usual repair practice to drill a notch at the vicinity of the crack in order to retard its propagation, by the increase in the radius of curvature at the tip of a propagating crack (Ref 49).

More analytically, the substrate was manufactured by eight layers of an MTM56 series prepreg provided by Advanced Composites Group (UK) (cure cycle: 30 min at 120 °C; reinforcement: woven carbon fabric; 199 g/m²). The laminate was cured according to the recommended curing cycle. 300 × 500 mm² coupons were cut and a Ø5-mm notch was subsequently drilled in the center of each coupon using a diamond drill.

The tapered CFRP patch was applied on the coupon and was manufactured using the 5H SATIN 43280 satin weave fabric (provided by HEXCEL). The fabric was impregnated at the recommended weight ratio with the Epocast 52 A/B (provided by Huntsman) modified with 0.5% w/w multi wall CNTs (provided by ARCHEMA) to enhance its electrical properties. As was established in preliminary studies, with efficient dispersion, electrical percolation is achieved at concentrations between 0.2 and 0.3%. The 0.5% w/w ratio was chosen for this study as (i) it is well above the percolation threshold and (ii) is low enough to retain the viscosity of the nano-reinforced matrix in a workable level.

The CNTs were dispersed in the epoxy matrix via sonication for 2 h using the ultrasonic processor UP400S (400 W, 24 kHz) by Hielscher at 50% amplitude. As is well known, ultrasonication may disperse the nanophase, but at the same time induces multiple breaks which reduce drastically the aspect ratio of the CNTs and as a consequence their reinforcing ability. The employed dispersion protocol was experimentally found to yield optimal fracture toughness properties for 0.5% w/w CNT/matrix ratio, without destroying the CNTs (Ref 50).

The patch was applied in layers using the conventional wet lay-up, using a tapered geometry in order to minimize the high shear stress fields at the edges of the repair. The pre-impregnated layer dimensions were $120 \times 50 \text{ mm}^2$ (1st ply), $100 \times 50 \text{ mm}^2$ (2nd ply), $80 \times 50 \text{ mm}^2$ (3rd ply), and $60 \times 50 \text{ mm}^2$ (4th ply) (Fig. 1). Curing of the patch on the substrate was performed in an autoclave as follows: (i) reaching 0.98 bar vacuum condition, (ii) increase of vacuum pressure to 6.2 bar, (iii) increase of temperature at $120 \text{ }^\circ\text{C}$ with $3 \text{ }^\circ\text{C}/\text{min}$ rate, (iv) retaining stable vacuum pressure and temperature for 10 min, (v) decrease of temperature at $80 \text{ }^\circ\text{C}$ with $-3 \text{ }^\circ\text{C}/\text{min}$ rate, and finally (vi) vacuum pressure release. In Fig. 1, the final

coupon configuration is depicted. Finally, $50 \times 60 \text{ mm}^2$ end tabs were attached on the composite coupons using high shear adhesive (Epibond 1590 A/B, Huntsman), in order to prevent failure at the gripping area.

3.2 Testing

For the EPCM measurements, electrically conductive contacts at specific locations were applied on the surface of the coupons using a conductive silver paint (Fig. 2). Commercially available silver paint and silver-loaded tape (RS-components) (Fig. 2a) were subsequently used in order to connect the cables of the multimeter (Agilent Technologies) connected to a PC for data acquisition and the DC power supply (XANDREX HPH 18-10DC). 150-mA direct current was injected in the specimen during mechanical loading and the electrical potential variation was concurrently recorded on both sides of the notch (V_A and V_B) (Fig. 2b).

As is shown in Fig. 2(b), the electrically conductive path between the substrate and the repair is formed through the patch/substrate interface. Apart from the conductive primary reinforcement, i.e., the carbon fibers, the electrical continuity between the repair and the substrate was enhanced in the transverse direction by the electrical conductive network formed by the CNTs in the matrix of the patch. As the conductive path includes the interface of the patch and the substrate, any changes in the form of debonding are expected to affect it directly. More analytically, as the debonding front propagates, the electrical potential values are expected to change monotonically. Thus, the evolution of the debonding during mechanical testing should result in the increase of the resistance or the potential drop between the measuring points.

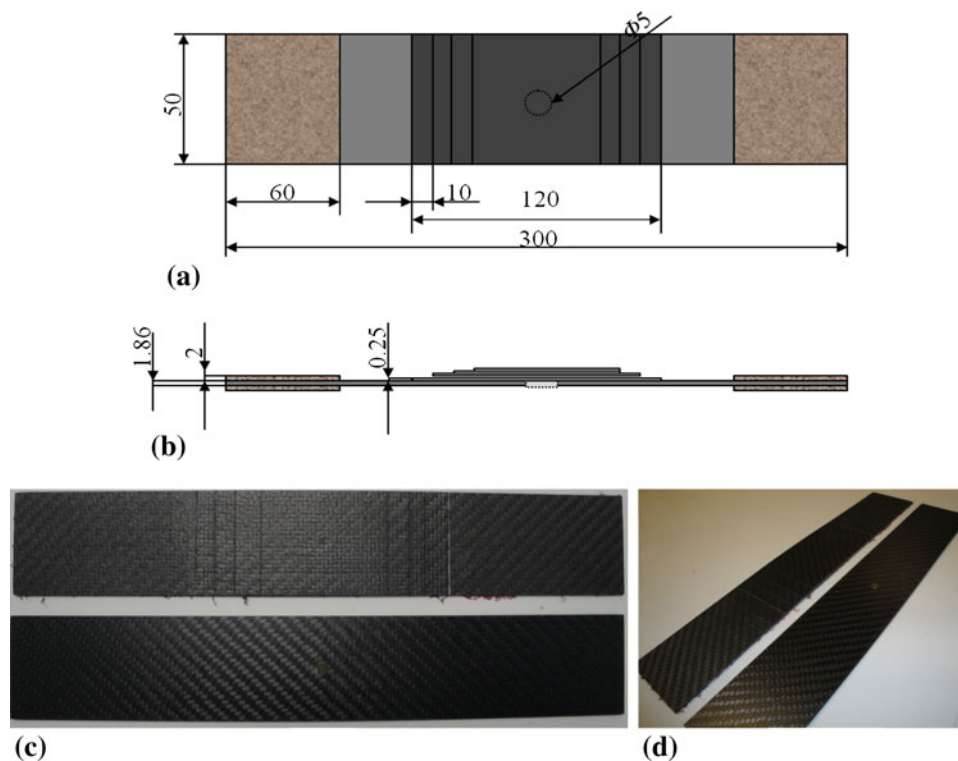


Fig. 1 (a, b) Schematic configuration of the employed specimen, (c, d) snapshots of both front (patched) and back side of the specimens

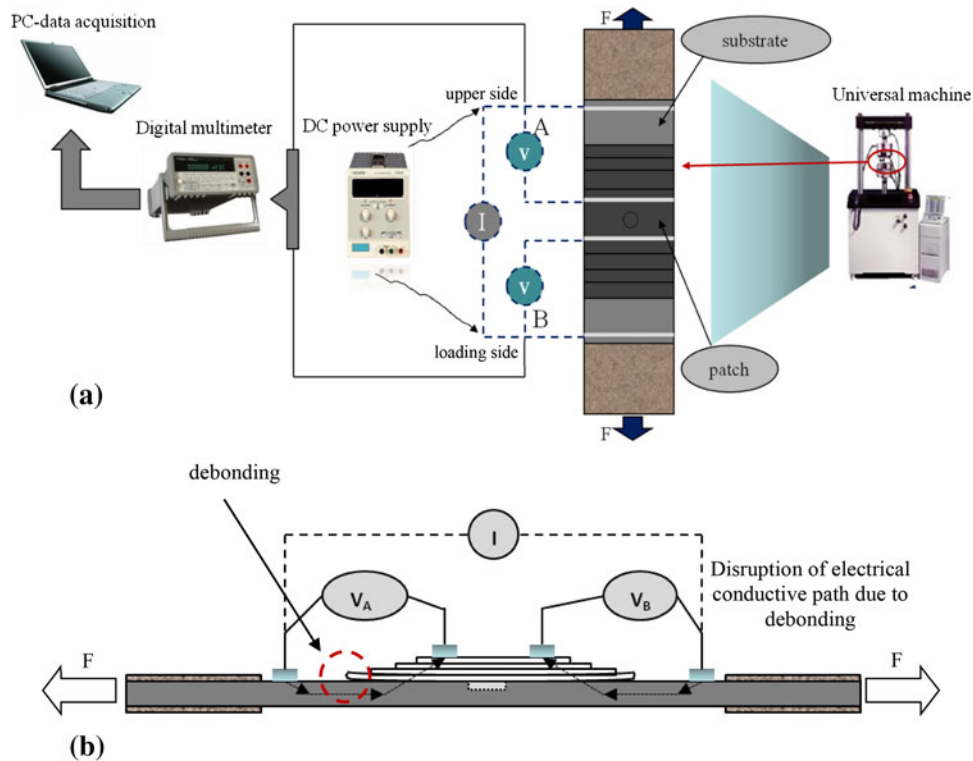


Fig. 2 (a) EPCM experimental setup, (b) EPCM measurement approach

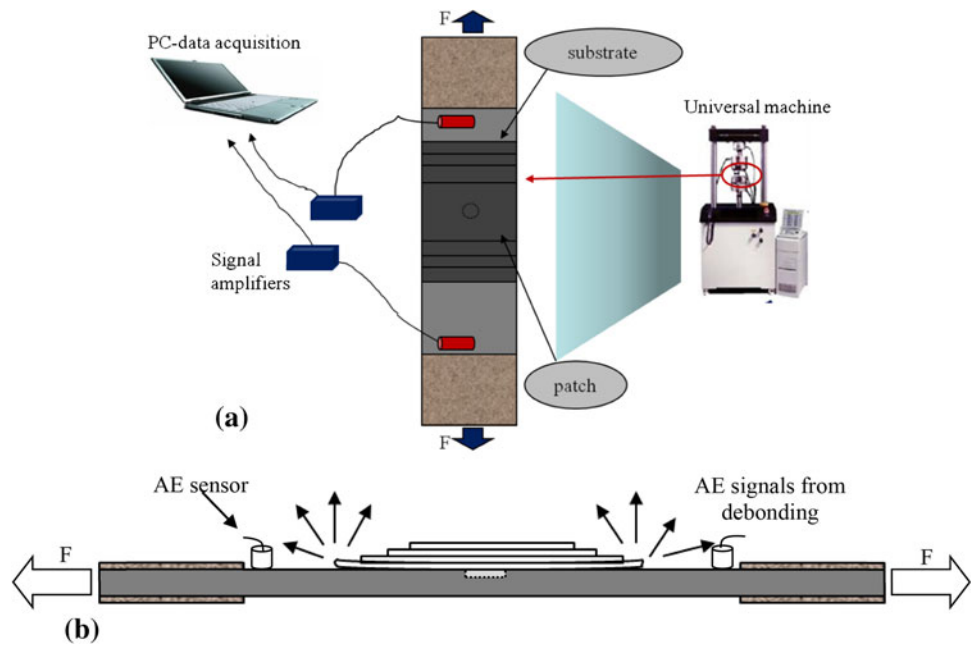


Fig. 3 (a) Schematic representation of AE technique, (b) AE signal measurement principle

For the AE monitoring, two broadband piezoelectric transducers (Pico, Physical Acoustics Corp., PAC) were attached on the specimen as shown in Fig. 3(a) and (b) at a specific distance (80 mm). Ultrasonic gel was applied for the acoustic coupling. The pre-amplifier gain was set to 40 dB. After performing a pilot test, the threshold was also set to 40 dB, in order to avoid electronic/environmental noise. The

signals were recorded employing a two-channel PCI-2 monitoring board of PAC with sampling rate of 5 MHz.

As is depicted in Fig. 3(b), the propagation of the patch debonding front causes the generation of AE hits. The simultaneous recording by the two broadband AE sensors allowed for the locating of the events due to debonding, along the length of the specimen. Thus, cumulative AE signals on

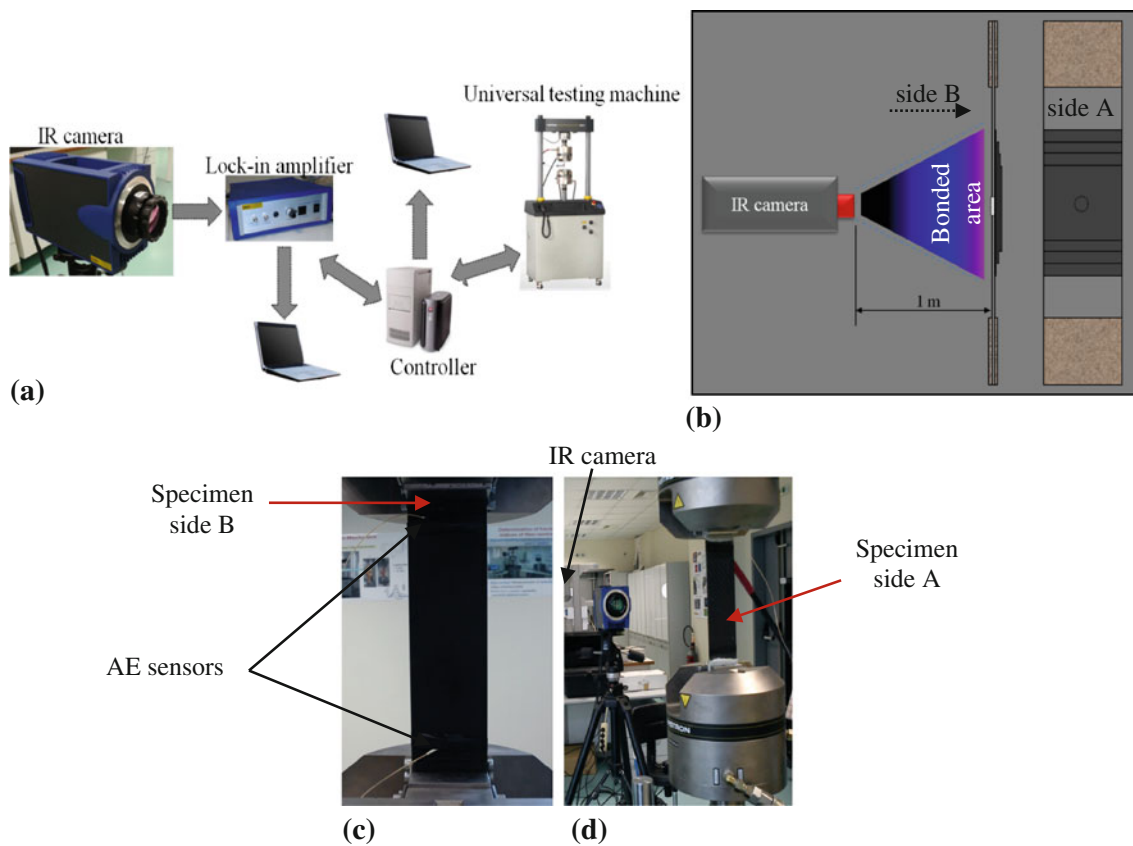


Fig. 4 (a) Schematic of the thermographic experimental setup, (b) recorded FOV of the thermal camera

either side of the patch along the loading axis may represent the length of the debonding front or the critical damage of the repaired material.

For the thermographic inspection, the Jade 510-CEDIP-MW infrared camera was used (Fig. 4). The camera employs a cooled indium antimonide (InSb) detector (3-5 μm), with a frame rate from 50-150 Hz and a focal plane array pixel format of 320×240 . The thermal sensitivity of the camera is lower than 25 mK at 25 $^{\circ}\text{C}$ and the resolution 0.001 $^{\circ}\text{C}$. The camera was employed in the lock-in mode at a frame frequency of 50 Hz. The cyclic loading imposed by the loading frame was 5 Hz. For the purposes of this work, the camera was positioned at approximately 1-m distance from the specimen in order to include the whole patched area in the field of view (FOV) of the camera (Fig. 4a, b). At this distance, the corresponding FOV was $208 \times 156 \text{ mm}^2$ with a lateral and perpendicular resolution of 0.65 mm/pixel. Figure 4(c) and (d) shows snapshots of the experimental setup of the second pair, IrT versus AE. In the aforementioned configuration, the cyclic loading is the source of thermal excitation of the material. As has been shown in a previous publication, debonding is manifested in the amplitude domain as a distinct discontinuity in the grayscale area, delineated by a hot zone which indicates the stress concentration at the debonding front.

The aforementioned inspection techniques were employed in pairs, as the current injection would interfere with the thermographic inspection. This is due to the fact that the Joule heating effect provoked by the current injection masks the heat generated either thermoelastically or due to irreversible damage. As should be noted at this point, the Joule effect can be utilized for damage monitoring. In a parallel study, the Joule effect has been successfully employed in conjunction with phase or LT to assess

delaminations in impacted composite panels (Ref 51). More analytically, the mechanical testing protocol included real-time monitoring of the fatigue loading by EPCM along with AE (1st pair) and IrT together with AE (2nd pair).

Prior to the application of the monitoring techniques, preliminary mechanical testing was performed in order to define the stress level at which stable debonding took place with the application of cyclic loading. To this end, the coupons were subjected to fatigue at incremental load levels for 20 kcycles at each level until stable debonding was observed. The debonding process was monitored thermographically online and assessed optically at the end of each load level increment, as was performed in Ref 26. Stable debonding was consistently observed for 80% of the static strength of the pristine laminate, as quoted by the manufacturer. A total of four coupons were tested in this load level (80%), two coupons with EPCM combined with AE monitoring and two coupons with thermography combined with AE monitoring.

Throughout the test campaign, a stress ratio of 0.1 and a 5-Hz frequency were adopted for the fatigue loading. All coupons failed consistently, starting with the progressive patch debonding of the patch from the side of the load application of the testing frame, the propagation toward the middle of the coupon, and the brittle transverse failure once the notch was revealed.

3.3 Results and Discussion

3.3.1 EPCM & AE. Figure 5 depicts the electrical potential changes (EPC) (Fig. 5a) and the acoustic activity (Fig. 5b) recorded during the fatigue mechanical testing of one of the two tested coupons as a function of the loading cycles.

The bottom side indicates the side at which the load was introduced by the loading frame. Both EPCM channels are depicted. The polarity was chosen so that increase in potential values corresponds to increase in the resistance of the monitored closed circuit, which would be the expected result from the propagation of the debonding front. With the selected formality, relative potential increase corresponds to increase in “potential drop” due to electrical resistance increase. AE activity snapshots are overlaid on the EPCM graphs indicating the location of the recorded events at specific instances during the experiment corresponding to the indicated EPCM measurements. The cumulative AE hits for the total duration of the experiment are shown in Fig. 5(b).

For both the top and the bottom side, the recorded noise is of a typical amplitude of 5 mV and high frequency. As was observed, this frequency is approximately 5 MHz which is indicative of the fact that it is not system noise, but corresponds to the real-time resistance fluctuations within individual fatigue cycles. The same phenomenon was observed in the case of fatigue of plain composite coupons (Ref 13). Additionally, there is a superimposed electrical potential oscillation of approximately 15-mV amplitude for 25 kcycles period, manifested as “drops” and “peaks” in the potential along the fatigue cycles. It may be postulated that these changes are attributed to

local disruptions of the electrical conductive path between the repair and the substrate mirroring the debonding evolution of the patch from the substrate. In this case, the patch should exhibit “stick-slip” behavior as critical failure progresses. Finally, there is a large-scale change with monotonic parts which is independent of the aforementioned oscillations. The discontinuity recorded at approximately 270 kcycles is not readily explained, but may be attributed to sudden change in a part of the electrical circuit independent of the interrogated repair, such as the contact resistance of the copper wires. The recorded large-scale EPC, as described in the previous paragraph, is distinctly different from the top to the bottom side. For both sides, the EPC exhibits a steep decrease in the initial few loading cycles. As should be noted, the initial potential value for both sides corresponds to the unloaded coupon. In this respect, the initial changes may be attributed to effects related to the local changes in contact resistance due to the initial cyclic loading. This monotonic potential decrease (which corresponds to resistance decrease) cannot be readily interpreted. However, similar effects have been recorded for the resistance change during step (Ref 7) or fatigue (Ref 52) loading. The initial decrease in the absolute potential values cannot be associated to damage, but relates to other mechanisms, which are activated during the first stages of the fatigue loading and may include

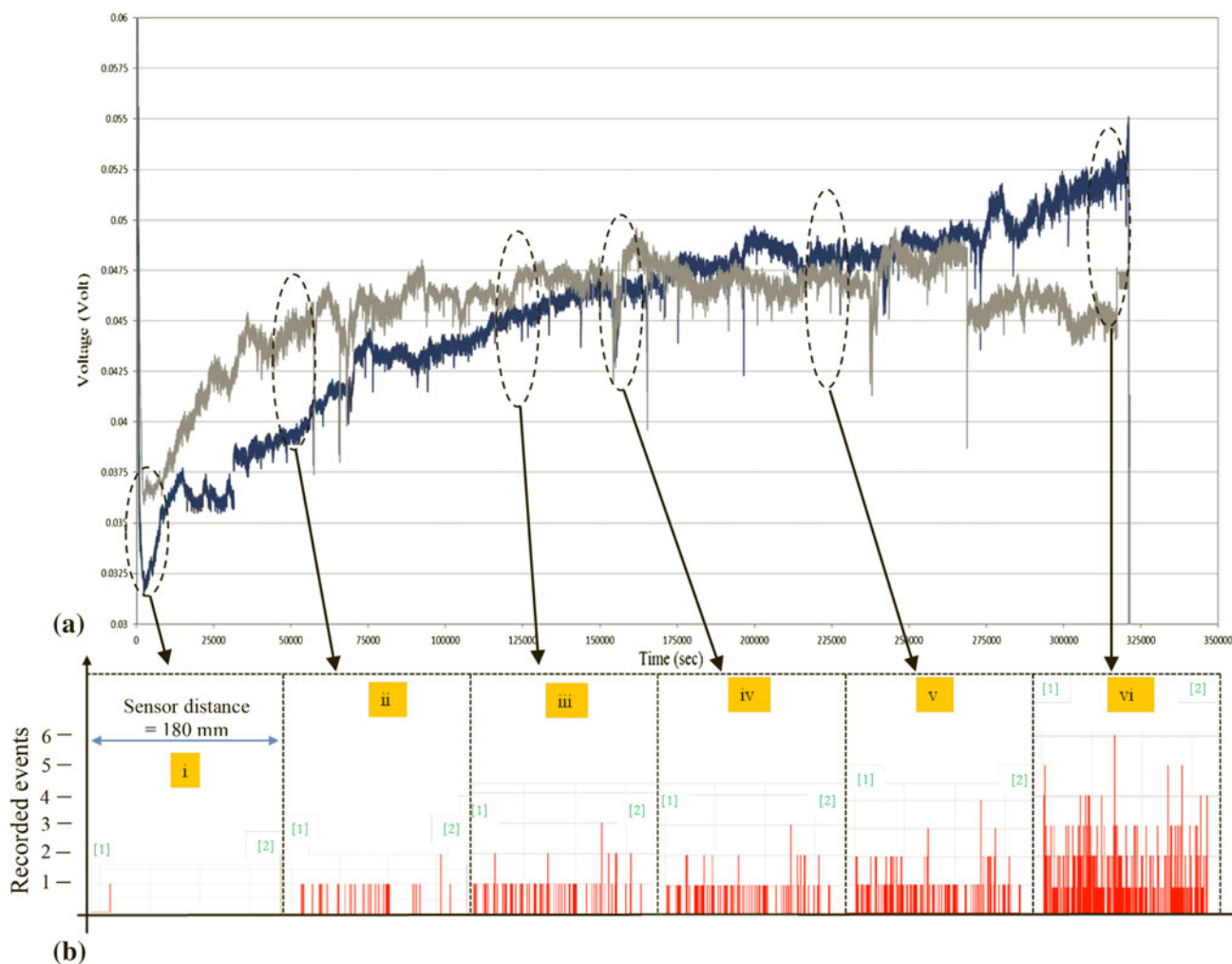


Fig. 5 (a) EPC along with (b) the AE signals during the fatigue mechanical testing

the increase of the 0° fiber alignment, the fiber piezo-resistive effect, the relaxation of the fiber pre-stressing, and the decrease of the contact resistance (Ref 52).

Following the aforementioned decrease, the EPC is differentiated from the top to the bottom channel. The top channel (gray line) exhibits a small increase in potential of approximately 10 mV from its minimum value and thereafter the potential values oscillate around a mean (0.045-0.047 V) value, suggesting the existence of the “stick-slip” mechanism which, however has reached a steady state. However, the EPC for the bottom channel exhibits a monotonic increase until the specimen failure. This increase is more than 30 mV from the minimum recorded value. The sudden potential drop at the end of the fatigue life obviously indicates loss of continuity due to specimen failure, which occurred with the critical failure of the bottom part of the patch followed by brittle transverse failure at the vicinity of the notch. Obviously, EPCM was successful in identifying the most probable failure site of the patch coupon, as after the initial stage, progressive critical failure was clearly manifested as monotonic potential increase of the bottom part of the coupon. The relative potential increase values as a function of fatigue life fraction for the bottom part of the coupon are shown in Fig. 6. Summarizing the aforementioned observations, EPCM (i) is capable of identifying the real-time resistance fluctuation within individual fatigue cycles, (ii) indicates the characteristic stick-slip behavior which relates to the progressive debonding of the patch due to fatigue, and most importantly (iii) is capable of clearly identifying the preferential side of failure of the patch.

As far as AE is concerned, the acoustic events as recorded at the same time with the electrical potential values are shown in Fig. 5(b). Snapshots of the cumulative acoustic events are presented as a function of the sensor positions. Events correspond to acoustic activity recorded within the time difference that sound travels within the length of the coupon. The differential arrival time allows for the calculation of the location of the sound source. The acoustic events which reflect the presence and location of damage start to appear from the edges of the repair (critical damage) moving along the center of the specimen indicating the debonding of the repair. As should be noted, the bottom part of the coupon (blue EPCM channel in

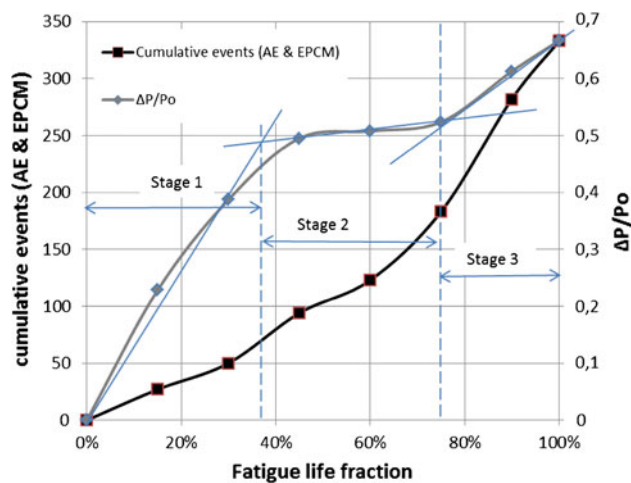


Fig. 6 Cumulative AE events and relative potential change as a function of fatigue life fraction; fatigue life stages that may be defined with EPCM are not obvious with AE

Fig. 5a) corresponds to the right side and the top part (gray EPCM channel in Fig. 5a) to the left side of the event location snapshots. The activity corresponding to the bottom channel appears consistently to be higher and this is indicative of the part where failure is most likely to take place. In the final stage of the test and prior to the final failure of the specimen, the recorded acoustic events are concentrated in the center of the specimen. At the same region, the coupon eventually failed due to the presence of the circular notch (subcritical damage). Summarizing, AE (i) is consistent with the observations made by EPCM and (ii) is capable of detecting subcritical failure at the end of the debonding process.

Figure 6 depicts the cumulative events as a function of fatigue life fraction together with the relative potential change recorded by EPCM as a function of fatigue life fraction. As can be easily observed, both techniques exhibit a monotonic increase. It may be postulated that three fatigue life stages may be defined with EPCM as indicated by the successive changes in the slope of the depicted curve, i.e., the onset of damage marked as stage 1, the increase in damage rate marked as stage 2, and finally the rapid deterioration that inevitably leads to failure (stage 3). AE is not as efficient in clearly identifying all stages of the fatigue life. As should be noted, the potential change is typical of a fatigue life diagram as in a typical fatigue case, stage 1 should exhibit a higher damage rate than stage 2. Finally, Fig. 7 depicts the cumulative events versus the relative potential change. This may be regarded as typical benchmarking or calibration graph for EPCM against AE. As can clearly be seen, the benchmarking scheme of both NDE methods is efficient in highlighting the fatigue stages with approximately linear interdependence for each fatigue life stage. Indicative of the potential of the benchmarking approach is that the fatigue life stages are more clearly defined in Fig. 7 than independently for both techniques (Fig. 6).

3.3.2 IrT & AE. In the second testing configuration, IrT was employed together with AE simultaneously to the mechanical testing. Amplitude images at specific load cycles are shown in Fig. 8. As was observed, debonding initiated at the 80% of the σ_{uts} . Hence, only amplitude images at that load level are presented (Fig. 8).

As is depicted in Fig. 8(a) to (h), stress concentration areas are present at the edges of the repair (critical damage) or at the

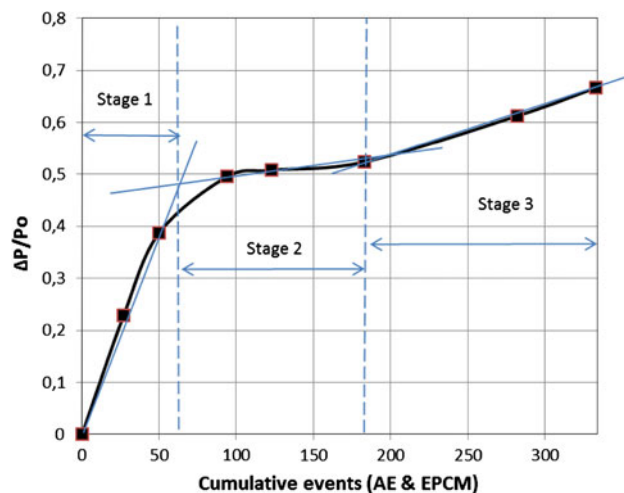


Fig. 7 Cumulative AE events vs. relative potential change

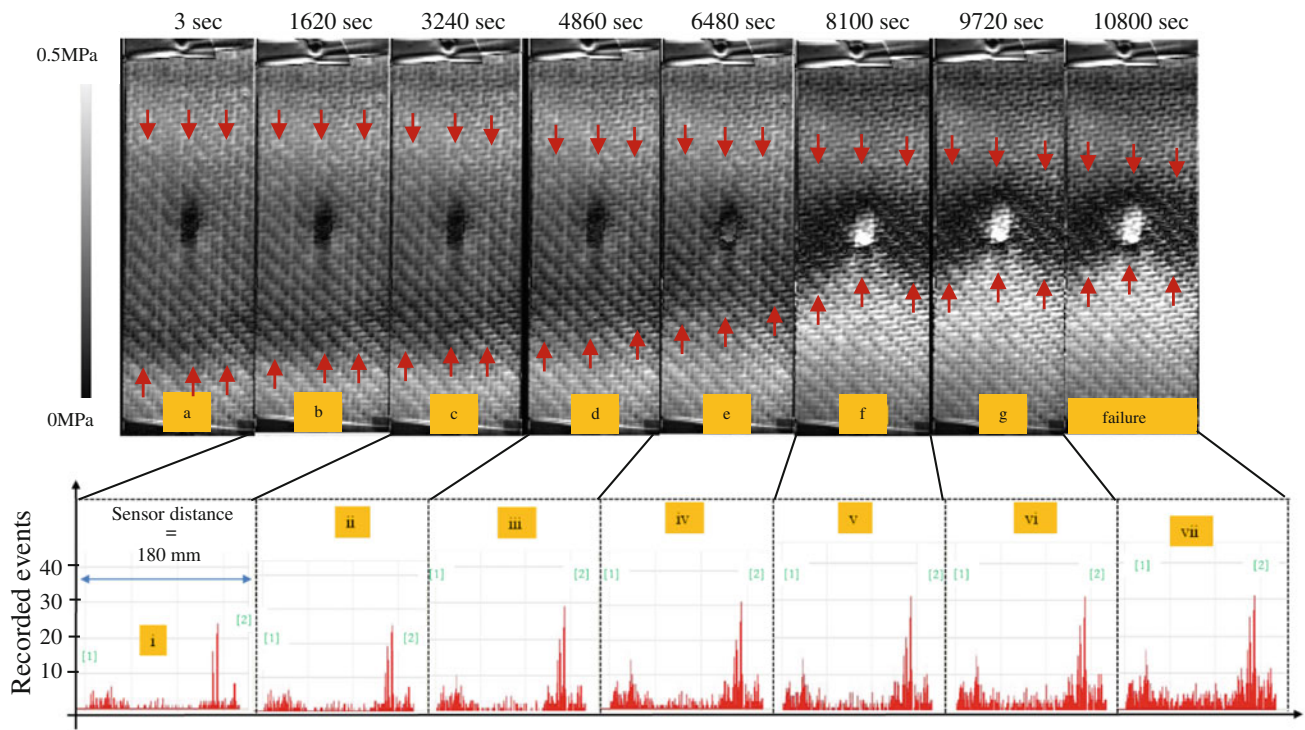


Fig. 8 Thermal images and acoustic events during fatigue mechanical loading at 80% of the σ_{UTS} of the substrate

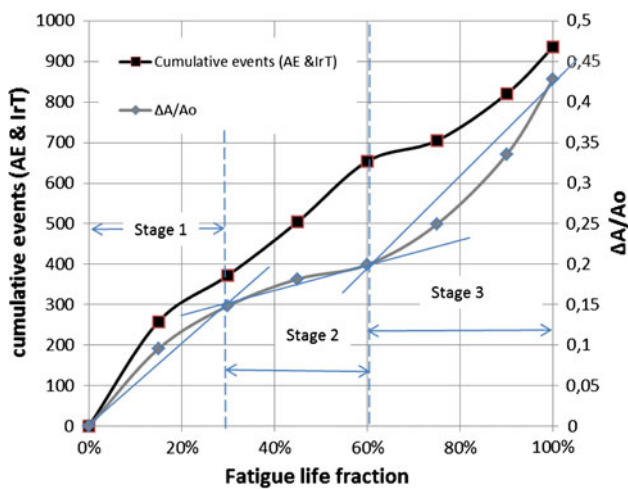


Fig. 9 Cumulative AE events and relative debonded area as a function of fatigue life fraction. Distinct fatigue life stages may be discerned with both methodologies

loci where high stresses are expected to appear and are manifested in the amplitude domain as regions of increased intensity (Ref 26). With fatigue loading, the high amplitude region is constricted from the bottom side toward the center of the specimen, implying that as debonding progresses, the debonded bottom area is practically relieved from stresses which are concentrated toward the middle of the coupon. As can be seen from the amplitude image series, the progress of critical damage of the coupon continued until the complete debonding of the bottom side of the repair from the substrate, which consistently failed in a transverse brittle manner at the

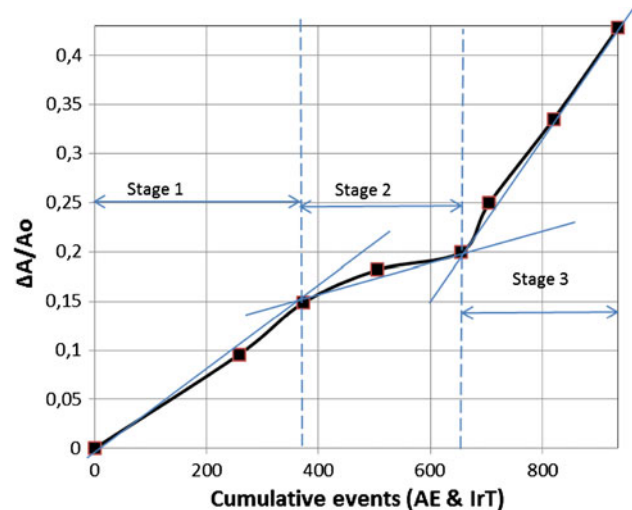


Fig. 10 Cumulative AE events vs. relative area change

notch edge. As is expected, the exposed “artificial” damage that is the circular notch caused a stress concentration leading to subcritical failure. The arrows on amplitude images show the direction of the patch debonding from the substrate.

Along with the thermal assessment, acoustic events were recorded at the same timing. In Fig. 8(i) to (vii), snapshots of the event location are presented for distinct cycles. As can be seen in Fig. 8(i), there is considerably more acoustic activity on the right-hand side which corresponds to the bottom part in the thermograph (Fig. 8a). As the fatigue progresses, the acoustic pattern is consistent (Fig. 8ii-vii) with considerably higher acoustic activity on the side where debonding is clearly

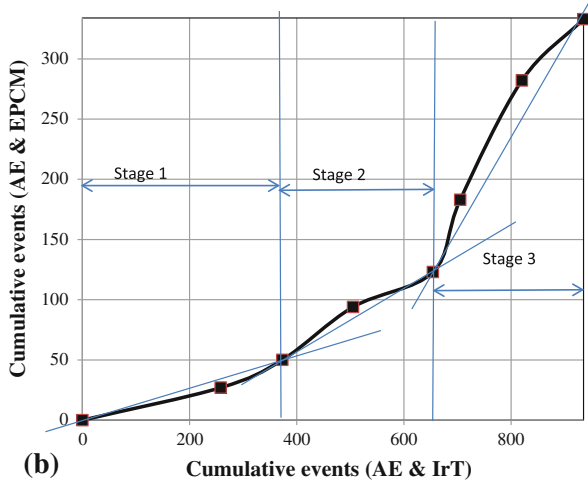
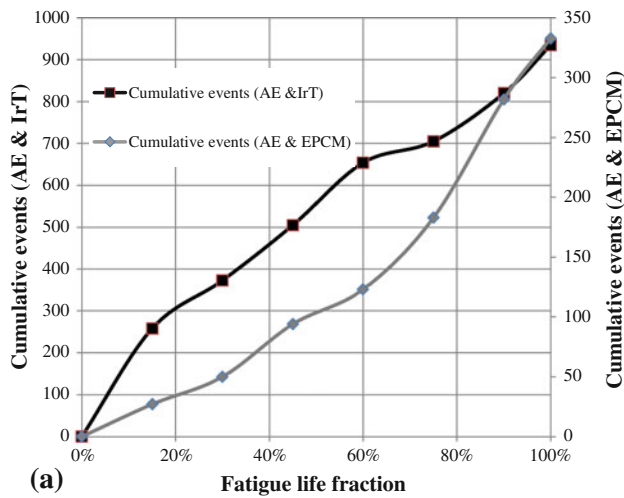


Fig. 11 (a) AE activity vs. lifetime fraction and (b) correlation of the cumulative events as recorded for the two distinct configurations

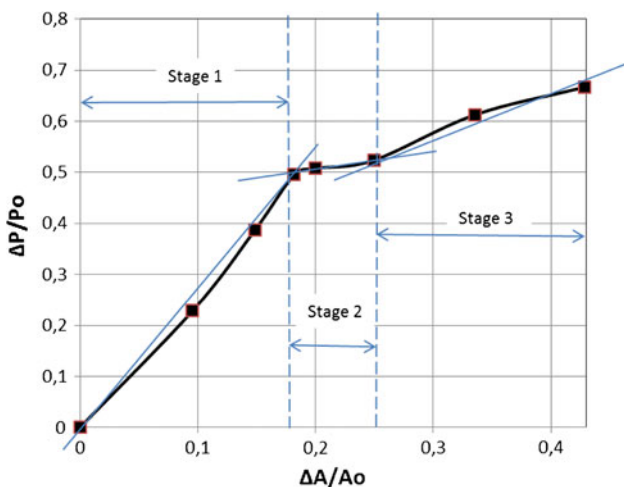


Fig. 12 Relative potential change vs. relative area change

discerned in the thermographic images (Fig. 8b-h). Additionally, in Fig. 8(i) to (vi), the acoustic events indicate that the debonding process initiated from the edges of the patch and

expanded toward the center of the specimen where the circular notch is present. To summarize, similar to the previous experimental configuration (EPCM & AE), there is more activity at the side which corresponds to the bottom part of the repaired coupon (in this representation corresponds to the right-hand side of the location snapshots). The distribution of the acoustic activity is indicative of the failure site and was confirmed by the catastrophic failure of the specimen; after the complete debonding of the bottom side of the patch from the substrate, the acoustic events appear to develop and basically concentrate around the loci of the artificial notch (in the middle of the specimen) until the catastrophic final failure of the coupon (subcritical failure). In this configuration as well, AE is able to identify the location of damage as well as to verify what was efficiently observed from the thermal assessment.

Figure 9 depicts both the relative debonded area and the recorded cumulative AE events versus the fatigue life fraction. As in the previous configuration, three distinct fatigue life stages are discernible with IrT, whereas this distinction is not obvious in AE. Again, the three fatigue stages as observed via the thermographic monitoring are typical of a fatigue life diagram, i.e., the initial fast damage progression stage (stage 1) is followed by a decreased rate (stage 2) and finally accelerates until failure (stage 3), indicating that the thermographic assessment provides a more reliable representation of damage which may also be readily quantified. This effect is more clearly depicted in Fig. 10, where the cross-correlation of the two methodologies is presented; in this representation, all three stages may be clearly defined, with the acoustic activity being directly proportional to IrT data for each consecutive stage.

3.3.3 Cross-Validation of the Applied NDE Techniques. Figures 6 and 9 clearly show that EPCM and IrT are capable of identifying three distinct fatigue stages. These stages are better highlighted when EPCM and IrT are interrelated with AE activity. In this way, the fatigue life stages are clearly defined. Interestingly enough though, the fatigue life stages are almost identical in the fatigue life fraction representation for the two studied configurations, i.e., stage 1 range ends at approximately 35-45% and stage 2 at approximately 60%. In other words, provided that the correlation between the AE activities in the two scenarios is satisfactory, an indirect cross-validation of IrT and EPCM may be performed; Fig. 11(a) depicts the AE activity versus lifetime fraction and Fig. 11(b) depicts the correlation of the cumulative events as recorded for the two distinct configurations. It is interesting to note that the fatigue life stages are clearly defined via the cross-correlation of the results for the two distinct configurations. Moreover, the cross-correlation of the acoustic activity for the two NDE scenarios presents an envelope which is directly relevant to the uncertainty provided by the indirect benchmarking of IrT versus EPCM as concurrent monitoring was not feasible with both techniques. Figure 12 depicts the benchmarking of IrT against EPCM; within the uncertainty of the approach, the indirect benchmarking of the two methodologies can be performed successfully in order to define the fatigue life stages as a function of the fatigue life fraction, providing a universal benchmarking for the two “incompatible” NDE methodologies (Fig. 12).

Summarizing, the estimations for the fatigue life stage transitions for all studied configurations and combinations are presented in Table 1.

Figure 13 depicts post-failure images (Fig. 13a-c) as well as stereoscopic (Fig. 13d) of a representative tested coupon. Longitudinal cracking (horizontal lines) on the surface of the

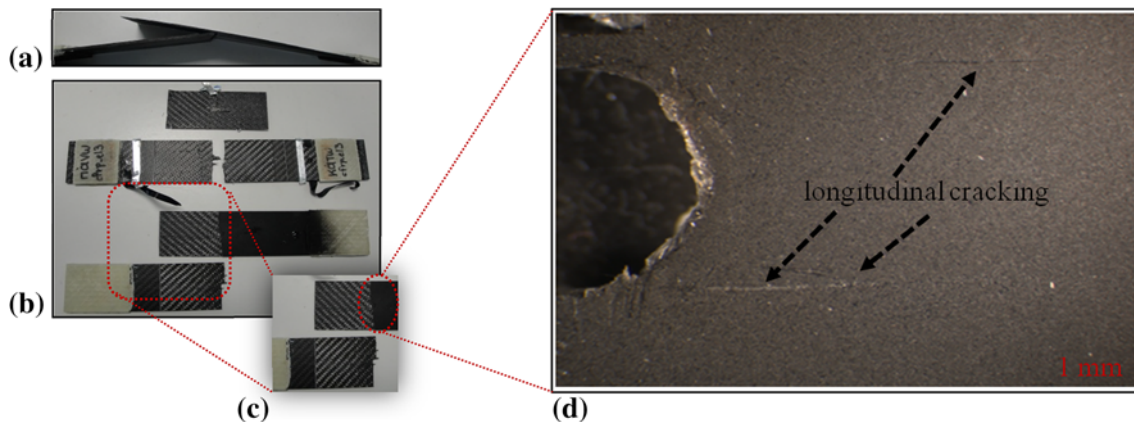


Fig. 13 (a, b, c) Post-failure images, (d) image taken via a stereoscope

Table 1 Fatigue life stage transition estimation

NDE methodologies	Stage 1 to stage 2 (35-45% of fatigue life time)	Stage 2 to stage 3 (55-65% of fatigue life time)
EPCM	☑	☑
AE (EPCM)	☒	☒
IRT	☑	☑
AE (IrT)	☒	☒
AE (EPCM) & AE (IrT)	☑	☑
EPCM & IrT	☑	☑

upper side of the broken specimen is visible in Fig. 13(d). The post-mortem images indicate the consistent type of failure as well as the characteristic behavior of the composite where longitudinal cracks blunt the stress concentration at the edge of the notch.

4. Conclusions

Within the scope of this paper, a combined NDE system was developed through EPCM, AE, and IrT for the monitoring of the repair integrity in composite repaired laminates with a central notch. The aim was to cross-validate and benchmark all involved methodologies. Critical and subcritical damage were efficiently identified and recorded during fatigue mechanical loading. Two scenarios were employed whereby the aforementioned techniques were employed in pairs, i.e., AE & EPCM and AE & IrT. The NDE methods were employed in real time simultaneously to the testing procedure. In all tested cases, the coupons failed in a consistent way, whereby critical failure initiated from one side of the specimen, was propagated toward the middle of the specimen, and exposed the notch, inducing thus transverse failure.

All techniques sufficiently identified the debonding process. Both EPCM and IrT indicated three well-defined stages along the fatigue life of the interrogated coupons. The fatigue stage transition was identified at ca. 40% for the first to the second stage and at ca. 60% for the second to third stage. EPCM was successful in clearly identifying the topology of the progressive debonding as denoted by the monotonic potential increase which was only observed at the side where critical failure initiated and propagated. Secondary effects that are observed in

the fluctuation of the electrical potential may be attributed to real-time strain variations due to fatigue and a characteristic stick-slip behavior which is not directly related to damage propagation. The concurrent AE monitoring partially revealed the directionality of the critical failure, as denoted by the increased activity on the failure side of the coupons. The correlation of the two techniques was very satisfactory and was feasible in enhancing the observed fatigue life stages.

The IrT technique was successful in identifying stress concentration areas at the edges of the repair which led to debonding from the substrate (critical failure). Stress concentrations were observed at either side of the circular notch. As fatigue loading continued, debonding was manifested by the restriction of high intensity areas in the amplitude domain toward the center of the specimen. The relative debonded area was calculated from the IrT thermographs. As mentioned before, three fatigue life stages were visible, which were found to correspond better to typical fatigue behavior, whereby the first stage possesses a higher gradient than the second and in the third, the damage rate is accelerated until failure. In general, the interrelation of the IrT and AE performed concurrently in real time during the loading of the coupon revealed a clear representation of the fatigue life stages.

Concluding, the EPCM technique is a promising technique for the assessment of the repair integrity via the identification of the potential failure site as well as the fatigue life stages of the tested component. The same conclusion is valid for IrT which also provides a real-time 2D visualization of the critical failure. The cross-correlation of the employed methodologies revealed that the monitoring of the fatigue behavior may be enhanced via the combination of the proposed methods on a single platform. It was shown that the correlation may be very good and provide the estimation of the distinct fatigue life stage transitions when plotted against lifetime fraction. The consistency of the failure process with well-defined transitions at fractions of the fatigue life time in all studied configurations allowed for an indirect correlation of the IrT and the EPCM methods.

References

1. D Hull and TW Clyne, *An Introduction to Composite Materials*. Cambridge University Press, New York, 1996
2. G Lubin and ST Peters, *Handbook of Composites*. Chapman & Hall, London, 1998

3. AA Baker, Repair of Cracked or Defective Metallic Aircraft Components with Advanced Fibre Composites—An Overview of Australian Work, *Compos. Struct.*, 1984, **2**(2), p 153–181
4. CL Ong and SB Shen, The Reinforcing Effect of Composite Patch Repairs on Metallic Aircraft Structures, *Intl. J. Adhesion Adhesives*, 1992, **12**(1), p 19–26
5. AA Baker, Fibre Composite repair of Cracked Metallic Aircraft Components—Practical and Basic Aspects, *Composites*, 1987, **18**(4), p 293–308
6. J Aghazadeh Mohandesi and B Majidi, Fatigue Damage Accumulation in Carbon/Epoxy Laminated Composites, *Mater. Des.*, 2009, **30**(6), p 1950–1956
7. SA Grammatikos and AS Paipetis, On the Electrical Properties of Multi Scale Reinforced Composites for Damage Accumulation Monitoring, *Compos. B*, 2012, **43**(6), p 2687–2696
8. JC Abry, S Bochart, A Chateauinois, M Salvia, and G Giraud, In Situ Detection of Damage in CFRP Laminates by Electrical Resistance Measurements, *Compos. Sci. Technol.*, 1999, **59**(6), p 925–935
9. N Angelidis, et al., Experimental and Finite Element Study of the Electrical Potential Technique for Damage Detection in CFRP Laminates, *Smart Mater. Struct.*, 2005, **14**(1), p 147,
10. A Vavouliotis, P Karapappas, T Loutas, T Voyatzis, A Paipetis, and V Kostopoulos, Multistage Fatigue Life Monitoring on Carbon Fibre Reinforced Polymers Enhanced with Multiwall Carbon Nanotubes, *Plast. Rubber Compos.*, 2009, **38**(2–3), p 124–130
11. S.A. Grammatikos and A.S. Paipetis, Electrical Resistance and Electrical Potential Studies for the Detection and Monitoring of Damage in Hybrid Composites, *Emerging Technologies in Non-destructive Testing V*, CRC Press, Boca Raton, 2012, p 401–406
12. G Sotiriadis, P Tsotra, A Paipetis, and V Kostopoulos, Stiffness Degradation Monitoring of Carbon Nanotube Doped Glass/Vinylester Composites via Resistance Measurements, *J. Nanostruct. Polym. Nanocompos.*, 2007, **3**(3), p 90–95
13. A Vavouliotis, P Karapappas, T Loutas, T Voyatzis, A Paipetis V Kostopoulos, Multistage Fatigue Life Monitoring on Carbon Fibre Reinforced Polymers Enhanced with Multiwall Carbon Nanotubes, *Plast. Rubber Compos.*, 2009, **38**(2–4), p 124–130
14. V Kostopoulos, P Karapappas, T Loutas, A Vavouliotis, A Paipetis, and P Tsotra, Interlaminar Fracture Toughness of Carbon Fibre-Reinforced Polymer Laminates With Nano- and Micro-Fillers, *Strain*, 2011, **47**, p e269–e282
15. J Robertson, Realistic Application of CNTs, *Mater. Today*, 2004, **7**(9), p 46–52
16. VN Popov, Carbon Nanotubes: Properties and Application, *Mater. Sci. Eng. R*, 2004, **43**(3), p 61–102
17. W Jia, R Tchoudakov, E Segal, M Narkis, and A Siegmann, Electrically Conductive Composites Based on Epoxy Resin Containing Polyaniline-DBSA- and Polyaniline-DBSA-Coated Glass Fibers, *J. Appl. Polym. Sci.*, 2004, **91**(2), p 1329–1334
18. M Oyharçabal, T Olinga, MP Foulc, and V Vigneras, Polyaniline/Clay as Nanostructured Conductive Filler for Electrically Conductive Epoxy Composites. Influence of Filler Morphology, Chemical Nature of Reagents, and Curing Conditions on Composite Conductivity, *Synth. Met.*, 2012, **162**(7–8), p 555–562
19. V Kostopoulos, A Vavouliotis, P Karapappas, P Tsotra, and A Paipetis, Damage Monitoring of Carbon Fiber Reinforced Laminates Using Resistance Measurements. Improving Sensitivity Using Carbon Nanotube Doped Epoxy Matrix System, *J. Intell. Mater. Syst. Struct.*, 2009, **20**(9), p 1025–1034
20. A Todoroki, Delamination Monitoring Analysis of CFRP Structures Using Multi-Probe Electrical Method, *J. Intell. Mater. Syst. Struct.*, 2008, **19**(3), p 291–298
21. A Todoroki, Y Samejima, Y Hirano, and R Matsuzaki, Piezoresistivity of Unidirectional Carbon/Epoxy Composites for Multiaxial Loading, *Compos. Sci. Technol.*, 2009, **69**(11–12), p 1841–1846
22. M Ueda and A Todoroki, Delamination Monitoring of Quasi-Isotropic CFRP Laminate Using Electric Potential Change Method, *Mod. Phys. Lett. B*, 2008, **22**(11), p 869–874
23. J-M Park, D-S Kim, S-J Kim, P-G Kim, D-J Yoon, and KL DeVries, Inherent Sensing and Interfacial Evaluation of Carbon Nanofiber and Nanotube/Epoxy Composites Using Electrical Resistance Measurement and Micromechanical Technique, *Compos. B*, 2007, **38**(7–8), p 847–861
24. Y Shindo, Y Kuronuma, T Takeda, F Narita, and SY Fu, Electrical Resistance Change and Crack Behavior in Carbon Nanotube/Polymer Composites Under Tensile Loading, *Compos. B*, 2012, **43**(1), p 39–43
25. ET Thostenson and TW Chou, Carbon Nanotube Networks: Sensing of Distributed Strain and Damage for Life Prediction and Self Healing, *Adv. Mater.*, 2006, **18**(21), p 2837–2841
26. SA Grammatikos, EZ Kordatos, NM Barkoula, TE Matikas, and AS Paipetis, Innovative Non-destructive Evaluation and Damage Characterisation of Composite Aerostructures Using Thermography, *Plast. Rubber Compos.*, 2011, **40**(6–7), p 342–348
27. EZ Kordatos, DG Aggelis, and TE Matikas, Monitoring Mechanical Damage in Structural Materials Using Complimentary NDE Techniques Based on Thermography and Acoustic Emission, *Compos. B*, 2012, **43**(6), p 2676–2686
28. R Steinberger, TI Valadas Leitão, E Ladstätter, G Pinter, W Billinger, and RW Lang, Infrared Thermographic Techniques for Non-destructive Damage Characterization of Carbon Fibre Reinforced Polymers During Tensile Fatigue Testing, *Int. J. Fatigue*, 2006, **28**(10), p 1340–1347
29. L Toubal, M Karama, and B Lorrain, Damage Evolution and Infrared Thermography in Woven Composite Laminates Under Fatigue Loading, *Int. J. Fatigue.*, 2006, **28**(12), p 1867–1872
30. DP Myriounis, EZ Kordatos, ST Hasan, and TE Matikas, Crack-Tip Stress Field and Fatigue Crack Growth Monitoring Using Infrared Lock-in Thermography in A359/SiCp Composites, *Strain*, 2011, **47** (Suppl. 1), p e619–e627
31. L Krstulovic-Opara, B Klarin, P Neves, and Z Domazet, Thermal Imaging and Thermoelastic Stress Analysis of Impact Damage of Composite Materials, *Eng. Fail. Anal.*, 2011, **18**(2), p 713–719
32. X. Maldague, Applications of Infrared Thermography in NonDestructive Evaluation, *Testing TiON*, P. Rastogi, Ed., *e-J. Nondestruct. Test. Ultrason.*, 2000, p 591–609
33. X Maldague, F Galmiche, and A Ziadi, Advances in Pulsed Phase Thermography, *Infrared Phys. Technol.*, 2002, **43**(3–5), p 175–181
34. C Meola and GM Carlomagno, Recent Advances in the Use of Infrared Thermography, *Meas. Sci. Technol.*, 2004, **15**(9), p R27–R58
35. C Meola, GM Carlomagno, A Squillace, and A Vitiello, Non-destructive Evaluation of Aerospace Materials with Lock-in Thermography, *Eng. Fail. Anal.*, 2006, **13**(3 Special Issue), p 380–388
36. VP Vavilov and S Marinetti, Pulsed Phase Thermography and Fourier-Analysis Thermal Tomography, *Russ. J. Nondestruct. Test.*, 1999, **35** (2), p 134–145
37. L Cheng and GY Tian, Surface Crack Detection for Carbon Fiber Reinforced Plastic (CFRP) Materials Using Pulsed Eddy Current Thermography, *IEEE Sens. J.*, 2011, **11**(12), p 3261–3268
38. R Kulkarni and O Ochoa, Transverse and Longitudinal CTE Measurements of Carbon Fibers and Their Impact on Interfacial Residual Stresses in Composites, *J. Compos. Mater.*, 2006, **40**(8), p 733–754
39. SFH Parker, M Chandra, B Yates, M Dootson, and BJ Walters, The Influence of Distribution Between Fibre Orientations Upon the Thermal Expansion Characteristics of Carbon Fibre-Reinforced Plastics, *Composites*, 1981, **12**(4), p 281–287
40. KF Rogers, DM Kingston-Lee, LN Phillips, B Yates, M Chandra, and SFH Parker, The Thermal Expansion of Carbon-Fibre Reinforced Plastics—Part 6 The Influence of Fibre Weave in Fabric Reinforcement, *J. Mater. Sci.*, 1981, **16**(10), p 2803–2818
41. P. Bremond, New Developments in Thermoelastic Stress Analysis by Infrared Thermography, *IV Pan-American Conference for Non-destructive Testing*, Buenos Aires, 2007
42. W Thomson, On the Dynamical Theory of Heat, *Trans. R. Soc. Edinb.*, 1853, **20**, p 261–283
43. CU Grosse and M Ohtsu, *Acoustic Emission Testing*. Springer, Heidelberg, 2008
44. VM Malhotra and NJ Carino, *Handbook on Nondestructive Testing of Concrete*. CRC, Boca Raton, 2004
45. VM Malhotra and NJ Carino, *Handbook on Nondestructive Testing of Concrete Second Edition*. Taylor & Francis, Boca Raton, 2003
46. DG Aggelis, NM Barkoula, TE Matikas, and AS Paipetis, Acoustic Structural Health Monitoring of Composite Materials: Damage Identification and Evaluation in Cross Ply Laminates Using Acoustic Emission and Ultrasonics, *Compos. Sci. Technol.*, 2012, **72**, p 1127–1133

47. DG Aggelis, NM Barkoula, TE Matikas, and AS Paipetis, Acoustic Emission Monitoring of Degradation of Cross Ply Laminates, *J. Acoust. Soc. Am.*, 2010, **127**(6), p EL246–EL251
48. TP Philippidis, VN Nikolaidis, and AA Anastassopoulos, Damage Characterization of Carbon/Carbon Laminates Using Neural Network Techniques on AE Signals, *NDT & E Intl.*, 1998, **31**(5), p 329–340
49. TR Brussat, Estimating Initiation Times of Secondary Fatigue Cracks in Damage Tolerance Analysis, *Fatigue Eng. Mater. Struct.*, 1983, **6**(3), p 281–292
50. G Gkikas, NM Barkoula, and AS Paipetis, Effect of Dispersion Conditions on the Thermo-Mechanical and Toughness Properties of Multi Walled Carbon Nanotubes-Reinforced Epoxy, *Compos. B*, 2012, **43**(6), p 2697–2705
51. S.A. Grammatikos, E.Z. Kordatos, T.E. Matikas, and A.S. Paipetis, Low-Velocity Impact Damage Identification Using a Novel Current Injection Thermographic Technique, *Proceedings of SPIE—The International Society for Optical Engineering*, Vol 8346, San Diego, CA, 2012
52. A Vavouliotis, A Paipetis, and V Kostopoulos, On the Fatigue Life Prediction of CFRP Laminates Using the Electrical Resistance Change method, *Compos. Sci. Technol.*, 2011, **71**(5), p 630–642